On Monami modes and scales of a flexible vegetation array in a laminar boundary layer ⊘

Jinyuan Ni (倪锦远) ⓘ ; Chunning Ji (及春宁) ✉ ⓘ ; Dong Xu (许栋) ⓘ ; Xing Zhang (张星) ⓘ ;
Dongfang Liang (梁东方) ⓘ

Check for updates

View Online

Export Citation

CrossMark

08 August 2023 02:15:50

On Monami modes and scales of a flexible vegetation array in a laminar boundary layer

View Online　　Export Citation　　CrossMark

Jinyuan Ni (倪锦远),[1] Chunning Ji (及春宁),[1,a] Dong Xu (许栋),[2] Xing Zhang (张星),[3,4]
and Dongfang Liang (梁东方)[5]

AFFILIATIONS

[1]State Key Laboratory of Hydraulic Engineering Simulation and Safety, Tianjin University, Tianjin 300072, China
[2]Key Laboratory of Hydrologic-Cycle and Hydrodynamic-System of Ministry of Water Resources, Nanjing 210024, China
[3]State Key Laboratory of Nonlinear Mechanics, Institute of Mechanics, Chinese Academy of Sciences, Beijing 100190, China
[4]School of Engineering Science, University of Chinese Academy of Sciences, Beijing 100049, China
[5]Department of Engineering, University of Cambridge, Cambridge CB2 1PZ, United Kingdom

[a]Author to whom correspondence should be addressed: cnji@tju.edu.cn

ABSTRACT

Flexible aquatic vegetation exists widely in nature and serves multiple hydro-environmental functions mainly through fluid–structure interactions. The waving motion of vegetation arrays, known as Monami, is predominantly governed by Kelvin–Helmholtz (KH) instability, and its characteristic scales, such as wave height and wavelength, are still being explored. In this paper, the interactions between a large array of flexible vegetations and a laminar boundary-layer flow are investigated using direct numerical simulation. The parameters used are the Reynolds number Re = 400, mass ratio $\beta = 1.0$, bending rigidity $\gamma = 0.04$–0.22, and gap distance $d = 0.4$–1.6. A low frequency in Monami is found to be related to the fluctuation frequency of the onset position of the KH instability, which leads to the identification of four different Monami modes: regular Monami, quasi-regular Monami A, quasi-regular Monami B, and irregular Monami. The influences of the bending rigidity and gap distance on the Monami modes, KH instability onset position, and Monami characteristic scales are discussed. It was found that the causes of spatial and temporal variations in the characteristic scales of Monami vary depending on the mode. In the regular Monami mode, these variations result from the evolution of the KH vortex. In the quasi-regular Monami A mode, they are strongly affected by the shifting of the onset position of the KH instability. In the other two modes, these variations are caused by a combination of the fluctuation in the KH instability onset position and the complex interaction between vortices.

Published under an exclusive license by AIP Publishing. https://doi.org/10.1063/5.0155506

I. INTRODUCTION

Widely existing in natural rivers and lakes, aquatic vegetations are an integral part of the aquatic ecosystem and provide a wide range of ecosystem services. For example, they provide food and habitat for other organisms,[1] change the sediment transport,[2] and purify water bodies.[3] In addition, they also play an important role in ecological protection engineering, since they can be used to weaken waves,[4] reduce coastal erosion,[5] and protect submarine pipelines.[6] Aquatic vegetations achieve their multiple functions mainly through the interactions with the fluid flow, i.e., fluid–structure interactions (FSI). Under certain conditions, flexible vegetation arrays exhibit coherent waving motions, and this wave-like motion is widely observed in both terrestrial and aquatic plants. This phenomenon is known as Monami in aquatic plants and Honami in terrestrial plants.[7,8] It is generally accepted that

the dominant factor in the Monami phenomenon is mixing layer instability or Kelvin–Helmholtz (KH) instability.[9] In order to better understand the mechanisms of such interactions, it is necessary to investigate the dynamic responses of vegetations and flow features of fluid under various conditions, such as the Reynolds number, vegetation properties (bending rigidity, mass ratio, etc.), and distribution sparsity. In recent years, using simplified models, such as filaments, flaps, and plates, the relevant studies from different perspectives have been conducted theoretically,[10,11] experimentally,[12–15] and numerically.[16–20] A comprehensive review of this topic can be found in Nepf.[21]

Under different conditions, flexible vegetation can display a range of oscillation characteristics, resulting in different vortex structures observed in the flow field. Therefore, researchers have classified

different dynamic modes. Jin et al.[15] focused on the dynamics of wall-mounted flexible plates under inclined flows and experimentally identified three distinct modes of tip oscillation in different Cauchy numbers (the ratio between the hydrodynamic force on the vegetation and the vegetation elastic restoring force) and flow inclination angles. Zhang et al.[17] found three dynamic modes, namely, lodging, regular VIV (vortex-induced vibration), and static reconfiguration for a single-filament system in the laminar boundary layer and additionally identified a cavity oscillation mode for a dual-filament system. Wang et al.[22] investigated the interactions of single, double, and triple plates with the incoming Poiseuille flow and revealed the effects of bending rigidity and spacing on the dynamic modes and vortex structures. Chen et al.[18] extended the study of Wang et al.[22] by performing three-dimensional simulations.

As the number of plants increases to form arrays, the dynamic behaviors of the array become more complex. O'Connor and Revell[16] found that vegetation arrays show four patterns at different bending rigidities and mass ratios: static, flapping, regular waving, and irregular waving. Fang et al.[23] suggested that the imbalance between the development of mixing layer instability and the dissipation of vegetation response causes temporal and spatial variations in the waving amplitude of vegetation, leading regular waving to irregular waving. However, the associated mechanisms behind the transition are still unclear. In addition to the above four patterns, a new pattern called "dual," which is a natural combination of both flapping and waving, appears in Fang et al.[23] Zhang et al.[19] studied the dynamic modes of an array of plates in a laminar boundary flow at different values of bending rigidity and gap distance and found modes named static reconfiguration, sectional waving (periodic and quasiperiodic), regular waving (periodic and quasiperiodic), upright oscillation, and cavity oscillation. In fact, the sectional waving found by Zhang et al.[19] and the "dual" found by Fang et al.[23] are the same mode. Xu et al.[24] studied the dynamic response of an array of flexible slender rods in turbulent open channel flow and found that in longer and narrower open channels, rod arrays can exhibit two interesting types of impulsive wave motion, namely, the α and β modes. The α mode is the serpentine wave motion of the vegetation in the cross-flow direction, while the β mode is the periodic gathering–diverging behaviors of vegetation.

The phenomenon of frequency lock-in in different modes has also been extensively explored, and the relationship among oscillation frequency, natural frequency, and KH instability frequency has been discussed. For the single-filament and dual-filament systems,[17] the oscillation frequency is locked onto the second natural frequency in the regular vortex-induced vibration mode, while the oscillation frequency is locked onto the first natural frequency in the cavity oscillation mode. For vegetation arrays, Ghisalberti and Nepf[9] performed experiments, which indicate strong correlations between the waving frequency, velocity spectrum peak frequency, and the predicted KH frequency. O'Connor and Revell[16] numerically investigated the waving interactions of a flexible vegetation array with an open channel flow, and their results showed that regular waving mode occurs when the mean waving frequency of the array approaches the KH frequency. A disparity between the natural frequency of the array and the predicted KH frequency leads to transitions between different behavioral states. Fang et al.[23] found that the vegetation oscillation frequencies follow the first-order natural frequency in the waving branch and the second-order natural frequency in the flapping branch. The same conclusions

are also drawn in Zhang et al.[19] Moreover, in Fang et al.,[23] the lock-in effect is observed again between the KH frequency and the natural frequency of the array, and an attraction effect of the mixing layer is revealed.

All of the above-mentioned dynamic modes, except the static mode, are manifestations of instabilities. Recently, some studies have focused on the intensity of the mixing layer and the onset of instability. Zhang et al.[19] identified three flow instabilities that drive vegetation oscillation, with the KH instability being the source of excitation for the vegetation's waving branch. Using the drag coefficient amplitude to measure both the onset and scale of the coherent vortices, Fang et al.[23] found that increasing vegetation density increases the mixing layer strength and shifts the onset position of the mixing layer instability upstream. However, as vegetation density and bending rigidity further increase, the initial perturbation of the vegetation is suppressed, inhibiting the generation and development of mixing layer instability. Vieira et al.[25] studied the intensity of instability as a function of the Reynolds number and buoyancy parameter (where larger values indicate more rigid vegetation). The results showed that from the fluid perspective, the instability strength increases with increasing Reynolds number and buoyancy parameter, saturating for high values of both parameters. However, from the vegetation's perspective, the instability strength monotonically increases with increasing Reynolds number, but the maximum value of the instability strength occurs at an intermediate value of the buoyancy parameter. This means that vegetation with little flexibility can delay the onset of instability. However, there are few relevant studies, and the variations of the initial onset position of the KH instability with respect to the parameters remain unclear.

As mentioned earlier, the Monami phenomenon is a wave-like motion. Some scholars have studied the characteristic scales, such as wavelength, wave height, period, and wave phase velocity of Monami waves under different conditions. Patil and Singh[26] found through theoretical derivation that the amplitude and frequency of coherent waving of vegetations are closely related to the bending angle, height, diameter, and elasticity of the vegetation. Okamoto et al.[27] found experimentally that the number of flexible vegetations oscillating simultaneously in the Monami phenomenon depends on the length scale of the turbulence structure within the mixing layer, and that under their experimental conditions, large scale vortices almost simultaneously deflect four individuals. He et al.[28] simulated the dynamic response of vegetations at different Cauchy numbers and distribution densities and obtained the Monami scale as well as the phase velocity of the waves using wave number spectra and frequency-wave number spectra. Wang et al.[20] performed the fast Fourier transform to analyze the factors affecting the characteristics of Monami scales. They revealed that as the flow velocity increases, the Monami wavelength decreases, while the Monami amplitude (wave height) and Monami frequency increase. In addition, as the spacing increases, the Monami wavelength and Monami amplitude increase, while the Monami frequency decreases.

Despite the insights gained from previous studies, the dynamic behavior of a large array of flexible vegetations, especially the Monami phenomenon, and the associated mechanisms are still not fully understood. In particular, to the best of the authors' knowledge, no research has investigated the temporal and spatial fluctuations of the KH instability onset position quantitatively. Additionally, how the Monami

characteristic scales are affected by the fluctuation of this position is still unclear.

In this study, numerical simulations are carried out to investigate the interactions of an array of 100 flexible vegetations with a two-dimensional (2D) laminar boundary-layer flow. From the perspective of the KH instability onset position, four distinct Monami modes are classified, and the characteristics of these modes are discussed. The influences of bending rigidity and gap distance on the Monami instability are also explored. The spatial and temporal variations of the Monami characteristic scales in different modes are elucidated.

The rest of the paper is organized as follows: Sec. II describes the numerical methods and computational setup. Section III presents the results and main findings. Finally, Sec. IV draws the conclusions.

II. METHODOLOGY

A. Numerical methods

The flow field is solved using direct numerical simulation combined with the immersed boundary (IB) method. The incompressible Navier–Stokes and continuity equations that govern the fluid flow can be written as follows:

$$\frac{\partial \boldsymbol{u}}{\partial t} + (\boldsymbol{u} \cdot \nabla)\boldsymbol{u} = -\frac{1}{\rho_f}\nabla p + \nu\nabla^2 \boldsymbol{u} + \boldsymbol{f}, \tag{1}$$

$$\nabla \cdot \boldsymbol{u} = 0. \tag{2}$$

In these equations, $\boldsymbol{u}$ is the velocity vector, t is the time, p is the pressure, ρ_f is the fluid density, ν is the kinematic viscosity, and $\boldsymbol{f}$ is the extra body force that represents the actions of immersed objects on the fluid.

Vegetation is modeled as flexible plates, and the dynamics of individual vegetation are simulated using the Vector Form Intrinsic Finite Element (VFIFE) method. Based on point-value descriptions, the structure is discretized into a set of spatial nodes that are connected to each other by rod elements. The motion of each node J is used to describe the movement and deformation of the structure and satisfies Newton's second law,

$$m\dot{\boldsymbol{V}} + \zeta m\boldsymbol{V} + \boldsymbol{F}^{\text{int}} = \boldsymbol{F}^{\text{ext}},$$
$$I\dot{\boldsymbol{\omega}} + \zeta I\boldsymbol{\omega} + \boldsymbol{M}^{\text{int}} = \boldsymbol{M}^{\text{ext}}, \tag{3}$$

where m and I are the mass and moment of inertia matrix of the node, respectively. $\dot{\boldsymbol{V}}$, $\boldsymbol{V}$, $\dot{\boldsymbol{\omega}}$, and $\boldsymbol{\omega}$ are the acceleration, velocity, angular acceleration, and angular velocity of the node, respectively. $\boldsymbol{F}^{int}$, $\boldsymbol{F}^{ext}$, $\boldsymbol{M}^{int}$, and $\boldsymbol{M}^{ext}$ are the internal force, external force, internal moment, and external moment, respectively. ζ is the structural damping coefficient, which is set to zero in the present study. An explicit iterative scheme based on central differencing is utilized to solve Eq. (3) as follows:

$$\boldsymbol{x}^{n+1} = h_s^2 \frac{\boldsymbol{F}^{ext} - \boldsymbol{F}^{int}}{m} + 2\boldsymbol{x}^n - \boldsymbol{x}^{n-1},$$
$$\boldsymbol{\alpha}^{n+1} = h_s^2 \frac{\boldsymbol{M}^{ext} - \boldsymbol{M}^{int}}{I} + 2\boldsymbol{\alpha}^n - \boldsymbol{\alpha}^{n-1}, \tag{4}$$

$$\boldsymbol{V}^{n+1} = \frac{\boldsymbol{x}^{n+1} - \boldsymbol{x}^n}{h_s}, \quad \boldsymbol{\omega}^{n+1} = \frac{\boldsymbol{\alpha}^{n+1} - \boldsymbol{\alpha}^n}{h_s}, \tag{5}$$

where $\boldsymbol{x}$, $\boldsymbol{\alpha}$, and h_s denote the position of the node, the angle of rotation of the node, and the time step, respectively. The temporal trajectory of

any node on the structure is described by a set of time points, and the process between the time points is defined as a path element. Proper division of the path elements allows the properties of each node to be changed between two path elements, making the VFIFE method advantageous in modeling the discontinuous and nonlinear behavior of structures, such as large deformations, fractures, collapses, collisions, and penetrations. For more detailed information about the VFIFE method, readers are referred to Ting *et al.*[29,30] and Shih *et al.*[31]

The IB method is used to couple the fluid flow and structural deformation in the simulation. This method was first introduced by Peskin[32] in the simulation of blood flow in the human heart. In the IB method, the fluid variables are discretized on an Eulerian grid, which is Cartesian and fixed in space, while the structure is represented by a series of IB points on a Lagrangian grid, which is curvilinear and free to move. The main idea of the IB method is to satisfy the non-slip boundary conditions along the surface of the structure by introducing a force term in the fluid momentum equation. To discretize Eqs. (1) and (2), the second-order Adams–Bashforth time scheme and the second-order central differencing space scheme are used, which leads to the following conservation form:

$$\boldsymbol{u}^{n+1} = \boldsymbol{u}^n + \delta t\left(\frac{3}{2}\boldsymbol{\Pi}^n - \frac{1}{2}\boldsymbol{\Pi}^{n-1} - \frac{3}{2}\nabla p^n + \frac{1}{2}\nabla p^{n-1}\right) + \boldsymbol{f}^{n+\frac{1}{2}}\delta t, \tag{6}$$

$$\nabla \cdot \boldsymbol{u}^{n+1} = 0, \tag{7}$$

where $\boldsymbol{\Pi} = \nabla \cdot (-\boldsymbol{u}\boldsymbol{u} + \nu(\nabla \boldsymbol{u} + \nabla \boldsymbol{u}^T))$ is composed of the convective and diffusive terms, in which the superscript T is the transpose of a matrix. Superscripts $n+1$, $n+1/2$, n, and $n-1$ denote the time step. The extra body force can be calculated as

$$\boldsymbol{f}^{n+\frac{1}{2}}\delta t = D\left(\boldsymbol{v}^{n+1} - I\left(\boldsymbol{u}^n + \delta t\left(\frac{3}{2}\boldsymbol{\Pi}^n - \frac{1}{2}\boldsymbol{\Pi}^{n-1} - \frac{3}{2}\nabla p^n + \frac{1}{2}\nabla p^{n-1}\right)\right)\right), \tag{8}$$

where $\boldsymbol{v}^{n+1} = \boldsymbol{V}^{n+1} + \boldsymbol{r} \times \boldsymbol{\omega}^{n+1}$ is the desired velocity on the IB points obtained by solving Eq. (3), in which $\boldsymbol{r}$ is a vector from a node to an IB point. D and I are the distribution and interpolation functions, respectively, which are responsible for data transfer between the non-conforming Eulerian and Lagrangian grids. For the sake of conciseness, further descriptions of this method and its solution procedure can be found in our previous work.[33–39] Thanks to the advantages of the VFIFE and IB method, the present fully coupled and fully resolved FSI model is suitable for solving structures with large deformations and can reflect the realistic dynamic behaviors of vegetation array very well.

B. Computational setup

The schematic diagram of the computational model is shown in Fig. 1. An array of $V = 100$ flexible vegetations is clamped on the bottom surface, and each vegetation is indexed by n. Each vegetation element is of length L and thickness b and evenly spaced by a gap distance D. The inclination (tilt) angle θ is defined as the angle between the chord line and the vertical axis, given as $\theta = \arctan[\delta_x/(L + \delta_y)]$, where δ_x and δ_y are the tip displacements in the x and y directions, respectively. A uniform velocity of U_∞ is applied at the left entrance, and a laminar boundary-layer flow is developed along the

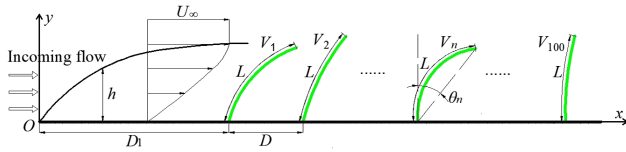FIG. 1. Schematic diagram of the computational model.

FIG. 2. Schematic diagram of the computational domain.

bottom surface with a varying thickness h. The distance between the inlet and the first vegetation is D_1, which is set to $16L$ in the present study. Four parameters, the Reynolds number Re, non-dimensional bending rigidity γ, mass ratio β, and the non-dimensional gap distance d, are considered here. They are defined as

$$\text{Re} = \frac{U_\infty L}{\nu}, \quad \gamma = \frac{EI}{\rho_f U_\infty^2 L^3}, \quad \beta = \frac{\rho_s b}{\rho_f L}, \quad d = \frac{D}{L}, \quad (9)$$

where E, I, b, and ρ_s are the Young's modulus, the moment of inertia of vegetation's cross section, the vegetation thickness, and the vegetation density, respectively.

With Reynolds number and mass ratio fixed, the ranges of the influencing parameters used in the simulations are summarized in Table I. The values of γ are from 0.04 to 0.22 in steps of 0.02, while the values of d are from 0.4 to 1.6 with an increment of 0.1 and 0.2 in the range of 0.4–1.2 and 1.2–1.6, respectively. These values were mainly selected based on the previous studies.[16,19,23] Our focus is on the ranges of parameters, in which the Monami, or waving mode, occurs, while the lodging, static, and flapping modes are beyond the scope of this paper.

As shown in Fig. 2, the computational domain is set as $[0, 204L]$ $\times [0, 8L]$ in the x and y directions. A non-uniform Cartesian mesh is employed in the simulations. In the subdomain of $[9L, 195L] \times [0, L]$ that contains all vegetations, grids with a width of $L/48$ in both x and y directions are used to resolve the small flow structures. The grids are stretched outside the subdomain with a stretching coefficient of 1.016 in the x direction and 1.030 in the y direction. In addition, the dimensionless time step ($\Delta t U_\infty / L$) is chosen carefully to satisfy the CFL (Courant–Friedrichs–Lewy) criteria ($\Delta t U_\infty / \Delta x < 0.5$). The boundary and initial conditions for the fluid flow and flexible vegetations are set as follows: For the fluid flow, Dirichlet boundary conditions ($u = U_\infty$, $v = 0$) are imposed on the inflow boundary, while Neumann boundary conditions ($\partial u/\partial x = \partial v/\partial x = 0$) are applied to the outflow boundary. The upper and bottom boundaries are set as free-slip ($\partial u/\partial y = 0$, $v = 0$) and non-slip ($u = 0$, $v = 0$) boundaries, respectively. For the clamped flexible vegetation, one end is fixed, while the other end is free. Initially, all vegetations stand vertically ($\theta = 0°$) with zero velocity.

Based on the Blasius solution for a laminar flow past a flat plate, the thickness of the boundary layer at the distance x from the entrance
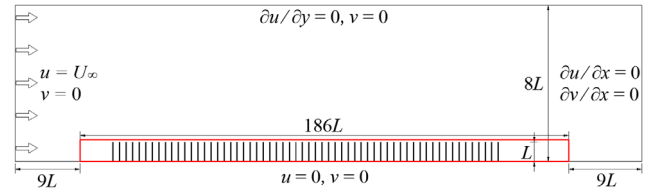
can be computed by $h = 5x/(\text{Re}_x)^{1/2}$, where $\text{Re}_x = U_\infty x/\nu$ represents the Reynolds number based on the distance from the entrance. The distance between the inlet and the first vegetation is $x = D_1 = 16L$, so $h_1 = L$, which means that the vegetation array is fully immersed in the boundary layer. The critical Reynolds number for the transition of a smooth flat plate based on the distance and incoming flow velocity is as high as $O(10^6)$.[40,41] In the present study, the largest Reynolds number at the exit is $\text{Re}_{\text{exit}} = U_\infty x/\nu = 81\,600$, which is far below the critical value. That is to say, the flow in the whole computational domain is 2D and laminar. Note that the existence of vegetation increases the flow instability and affects the critical Reynolds number. However, considering that Re_{exit} is two orders of magnitude smaller than the critical value, it is reasonable to consider the vegetation flow in the present study as laminar flow. In addition, the largest boundary layer thickness at the exit is $3.57L$, the Reynolds number based on which is around 1428.

It is also necessary to give a short description of the rationality of the 2D restriction used in this study. Compared to a real three-dimensional (3D) vegetation canopy, the blockage effect (i.e., the fluid is deflected upward due to the existence of vegetation) in a 2D model is enhanced owing to the fact that the out-of-plane flow around the vegetation is restricted. According to Nepf,[21] such a restriction is significant for terrestrial and deeply submerged canopies where the coherent flow structures are highly 3D because of their interactions with the boundary-layer turbulence. However, for shallowly submerged canopies like the setup presented in this study, the boundary layer is laminar and the coherent vortices (KH vortices) remain 2D in nature. Therefore, the 2D restriction here is reasonable, and such a simplification has been widely used in many similar researches.[16,17,19,23]

To verify the accuracy of the present numerical methodology, simulation results were compared with those of Zhang et al.[19] under the same conditions at Re = 400, $\gamma = 0.2$, $\beta = 1.0$, $d = 0.5$, and $V = 90$. The good agreement between the two sets of results shows that the present numerical methodology is accurate. Furthermore, tests were performed on both the number of vegetations in the array and the grid resolution to ensure a configuration-independent solution. Additional details are provided in the Appendix.

III. RESULTS AND DISCUSSION

A. Definition of instability onset position and Monami characteristic scales

Before proceeding further, we will first introduce how KH instability is present in vegetated flow and then define two important terms: the KH instability onset position and the Monami characteristic scales.

In the vegetated flow, due to the presence of vegetation, the vertical drag distribution is discontinued. As a result, the flow velocity

TABLE I. Influencing parameters applied in the simulations.

Parameters	Values
Reynolds number (Re)	400
Dimensionless bending rigidity (γ)	0.04–0.22
Dimensionless gap distance (d)	0.4–1.6
Mass ratio (β)	1.0

between the interstitial flow inside the canopy and the bulk flow above the canopy varies greatly, which causes an inflection point in the vertical velocity profile.[21] This inflection point makes the flow susceptible to KH instability, which leads to the generation of KH vortices[9] as shown in Fig. 3(a). In a free shear layer, KH vortices are symmetric around the inflection point and their convection speed matches the velocity at the inflection point. However, in a vegetated flow, the KH vortices are displaced higher than the inflection point and as a result, their convection velocity is higher than the velocity at the inflection point. In addition, due to the vegetation's drag, the vortices rotate more slowly than that formed in a free shear layer of comparable shear strength.[21]

The vegetation inclination angle's instantaneous amplitude is non-zero, where the mixing layer is unstable. According to Fang *et al.*,[23] the instability in the mixing layer arises due to the small oscillations of vegetation in the foremost part of the array. These oscillations are then amplified progressively downstream and eventually induce the KH instability. Therefore, the oscillation amplitude can be considered a measure of the mixing layer instability, while the KH instability is excited downstream when the oscillations are amplified to a certain extent, as shown in Fig. 3(a). Thus, we define the position where the fluctuation amplitude of the vegetation inclination angle first reaches at least 1° as the KH instability onset position,

$$n_o(t) = \left\{ n_o | \tilde{\theta}(n = n_o, t) \geq 1° \wedge \tilde{\theta}(n \leq n_o, t) < 1° \right\}, \quad (10)$$

where

$$\tilde{\theta}(n, t) = \theta(n, t) - \frac{1}{\Delta t} \int_{t_0}^{t_0 + \Delta t} \theta(n, t) dt. \quad (11)$$

Here, t_0 is selected to ensure the fully developed laminar boundary layer flow and statistically stable vegetation oscillations, while Δt is chosen long enough to capture the low-frequency oscillations. It should be noted that the selection of 1° has no physical significance, but changing its value slightly affects the onset position.

In the Monami motion, the envelope curve at the tip of the vegetation resembles a wave. To describe the wave characteristics, we define the crest and trough of the Monami wave,

$$crest(x_{n_c}, y_{n_c}, t) = \left\{ n_c | y_{n_c}(t) \geq y_{n_c-1}(t) \wedge y_{n_c}(t) > y_{n_c+1}(t) \right\},$$
$$trough(x_{n_t}, y_{n_t}, t) = \left\{ n_t | y_{n_t}(t) \leq y_{n_t-1}(t) \wedge y_{n_t}(t) < y_{n_t+1}(t) \right\}. \quad (12)$$

Consider that the crests and troughs of the Monami wave may not be exactly located at the vegetation tips. Therefore, a simple correction is applied: A parabola is fitted to the coordinates of the stem tips between which a crest (or trough) is located, and the coordinates of the vertex of this parabola define the position of the crest (or trough). Furthermore, we define the horizontal distance between two adjacent crests or troughs as the wavelength, and the vertical distance between the adjacent crest and trough as the wave height, as shown in Fig. 3(b). At any moment t, the array forms multiple wavelengths L_{m1}, L_{m2}, ..., and wave heights H_{m1}, H_{m2}, ..., and the mean wave height and mean wavelength during Δt can be calculated.

B. Characteristics of different Monami modes

In previous studies,[16,19,23] Monami patterns were divided into regular waving and irregular waving. Under regular waving, the vegetation oscillates at a single frequency, while under irregular waving, the vegetation oscillates at several different frequencies. In the present study, a low frequency component in the irregular waving mode is found to modulate the dominant frequency of the vegetation oscillations, causing the vegetations to oscillate at multiple frequencies. More importantly, this low frequency is found to be related to the fluctuation of the KH instability onset position.

In this section, the dynamic behaviors of the vegetation array with different bending rigidity and gap distance are systematically investigated. Based on the oscillatory characteristics of the KH instability onset position, four Monami modes, namely, regular Monami, quasi-regular Monami A, quasi-regular Monami B, and irregular Monami, are distinguished. The characteristics of these different modes are revealed and compared.

For the regular Monami mode, we take the case $\gamma = 0.2$, $d = 0.4$ as an example. Figure 4(a) shows the spatial and temporal variations in tilt fluctuations across the array, where each stripe represents a process in which a KH vortex is generated and gradually moves downstream, causing the vegetations to bend accordingly. The vertical distance between two adjacent stripes represents the oscillation period of the vegetations. It can be seen that in the regular Monami mode, the oscillation period of the vegetation remains constant. This is confirmed in Fig. 4(b), where the inclination angles of the selected vegetations vary regularly with time and the vegetations oscillate at a single dimensionless frequency of 0.2067. The solid black line in Fig. 4(a) indicates the contours for the instantaneous vegetation inclination
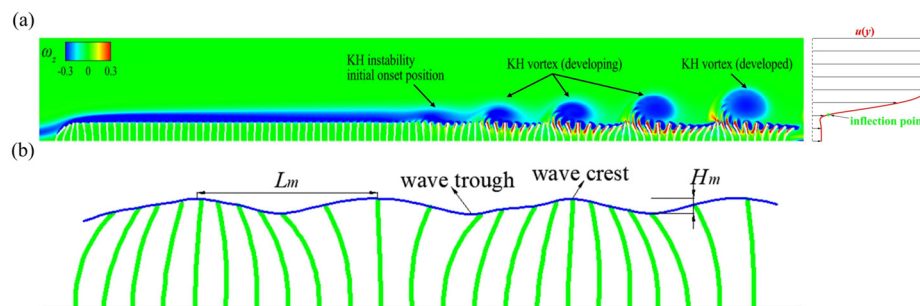

(a)

(b)

FIG. 3. (a) A contour of *z*-vorticity containing KH instability onset position and subsequent development of KH vortex. The vertical velocity profile *u*(*y*) with an inflection point is drawn at the KH instability initial onset position. (b) Schematic diagram of the wave-like motion, Monami, of the vegetation array and its characteristic scales, wavelength L_m, and wave height H_m. The green lines represent the vegetations. The Monami is represented by the blue envelope connecting the vegetation tips and travels to the right.
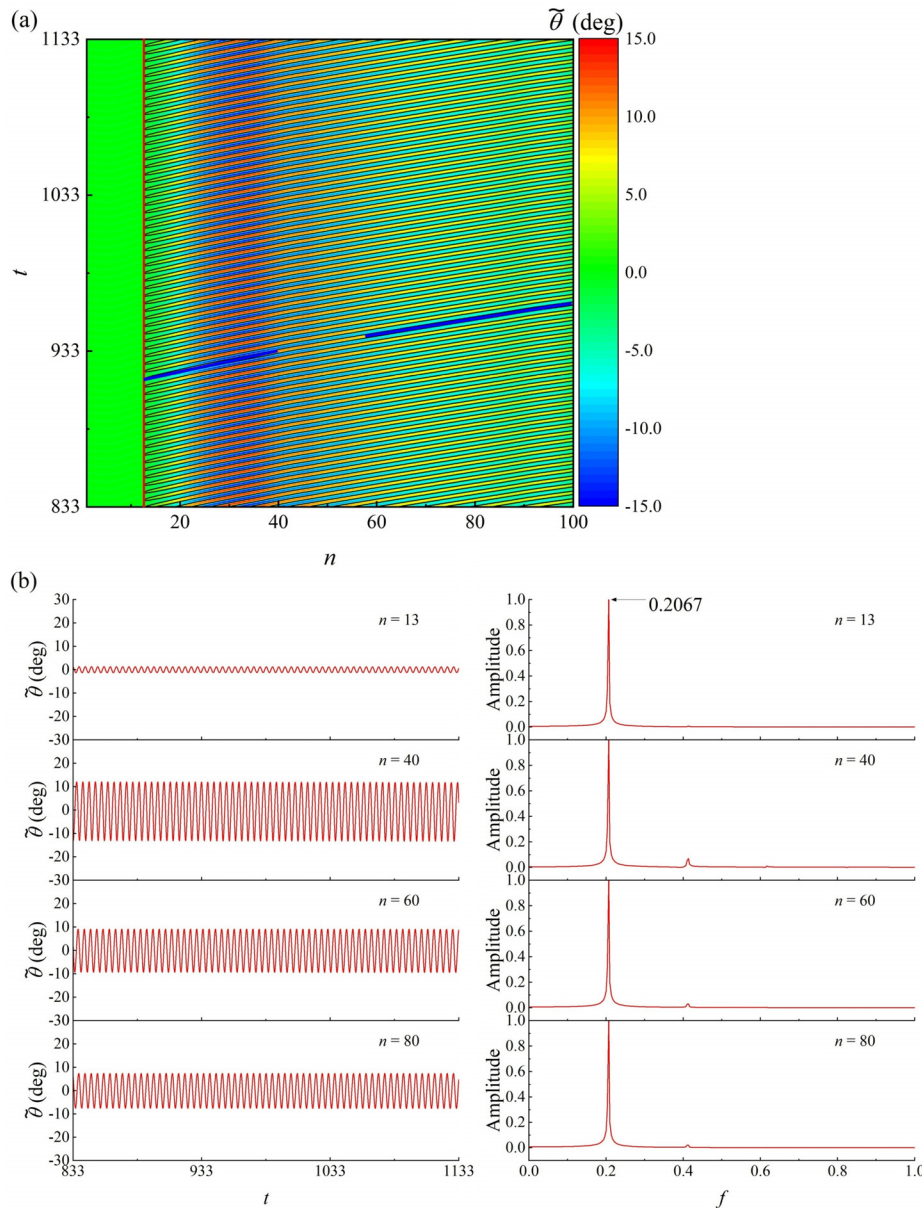
FIG. 4. (a) The spatial and temporal variations in tilt angle fluctuations across the array. The two solid blue lines indicate the same stripe in the upstream and downstream of the array. (b) Time histories and spectra of tilt angle fluctuations of representative vegetations ($\gamma = 0.2$, $d = 0.4$).

angle at $1°$. Based on the definition in Sec. III A, the KH instability onset position is located near $n = 13$, indicated by the red solid line. It is obvious that in the regular Monami mode, the KH instability onset position is fixed and does not vary with time, meaning that at any given moment, the KH vortex is excited at the same position and then propagates downstream. As a result, the KH vortices generated at different time instants have the same intensity when they propagate to the same position. Therefore, the vegetation at a given position oscillates with the same amplitude and frequency.

For the quasi-regular Monami A mode, the case $\gamma = 0.06$, $d = 0.6$ is taken as an example. Figure 5(a) shows the spatial and temporal variations in tilt angle fluctuations across the array, and again, by

definition, the KH instability onset position is determined as shown by the solid red line in the figure. It can be seen that in the quasi-regular Monami A mode, the onset position is no longer fixed, but moves upstream and downstream regularly with time. As the location of the instability excitation changes, the KH vortices excited at different time instants move downstream and pass the same position with different intensities, resulting in a periodic change in the oscillation amplitude of the vegetations. This is supported by the left column of Fig. 5(b), which shows the variations of the inclination angle and its upper envelope over time for representative vegetations. A fast Fourier transform of the tilt angle gives the spectra shown in the middle column of Fig. 5(b). It can be seen that the vegetations oscillate at several
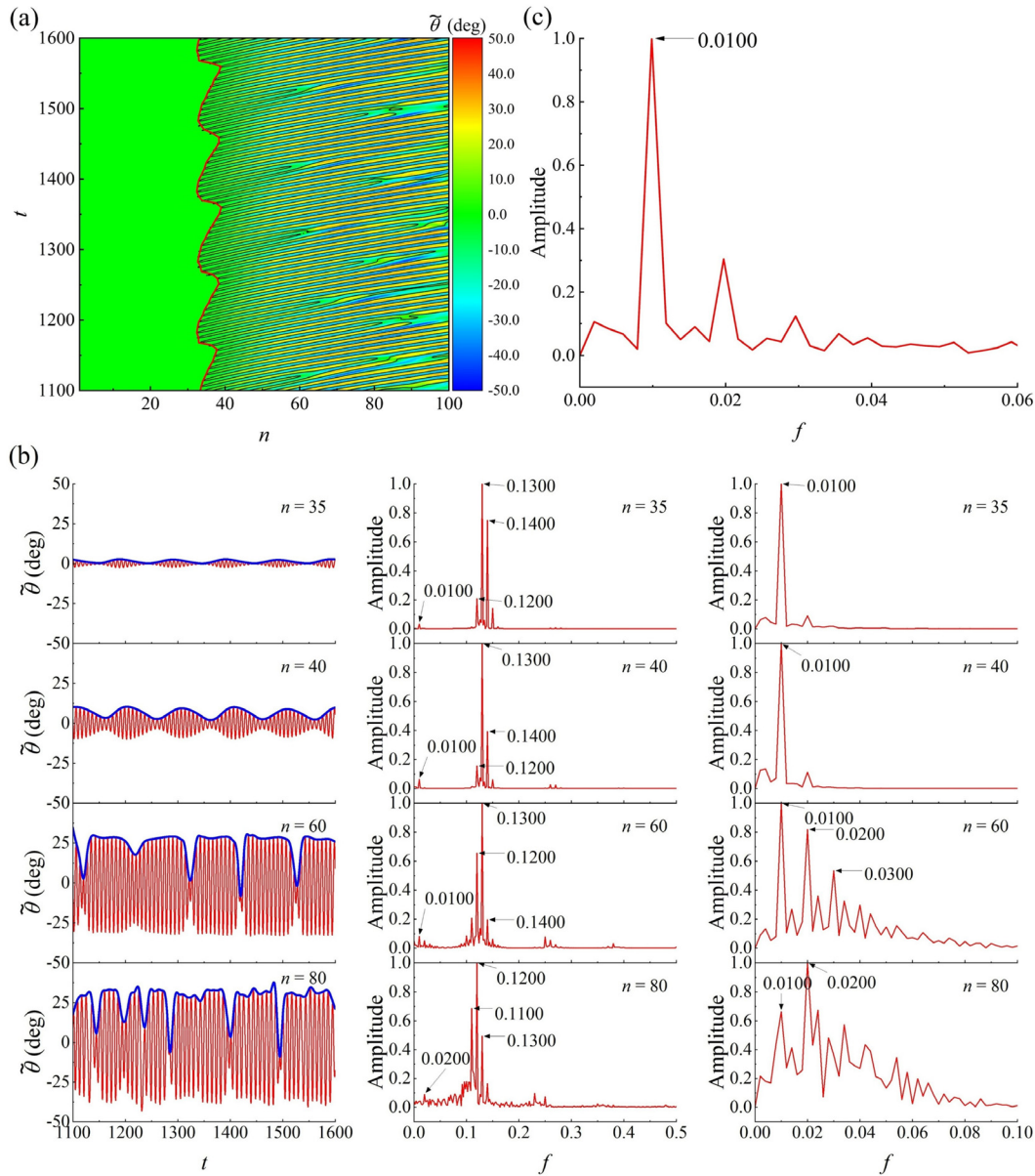
FIG. 5. (a) The spatial and temporal variations in tilt angle fluctuations across the array. (b) From left to right, the columns show time histories (solid red line) and upper envelope (solid blue line) of tilt angle fluctuations of representative vegetations, spectra of tilt angle fluctuations, and spectra of upper envelope of tilt angle fluctuations, respectively. (c) The spectrum of KH instability onset position ($\gamma = 0.06$, $d = 0.6$).

frequencies, including the dominant frequency of 0.1300, a low frequency of 0.0100, and other frequencies of 0.1100, 0.1200, and 0.1400. This is also reflected in Fig. 5(a), where the stripes show discontinuity regularly, matching the fluctuation pace of the KH instability onset position. Moreover, the frequencies 0.1100, 0.1200, and 0.1400 can be taken as the results of the nonlinear interactions of the dominant frequency 0.1300 and low frequency 0.0100. As shown in the right column of Fig. 5(b), it can be seen that the frequency of the upper envelope of the tilt angle f_{en}, i.e., the frequency of variation of the

vegetation oscillation amplitude, equals the low frequency in the middle column of Fig. 5(b). As mentioned earlier, the change in the vegetation oscillation amplitude is caused by the change in the KH instability onset position. The frequency spectrum in Fig. 5(c) shows that the dominant frequency of the KH instability onset position matches well the low frequency of the vegetation oscillation. In other words, in the quasi-regular Monami A mode, the oscillation of the vegetations is modulated by both its own oscillation frequency f_{vib} and the fluctuation frequency of KH instability onset position f_{onset}.

The periodic variation of the vegetation oscillation amplitude originates from the periodic variation of the instability excitation position, and the relationship $f_{onset} = f_{en}$ is satisfied.

In fact, the majority of quasi-regular Monami modes studied in our research do not show regular variation of instability excitation positions within the parameter ranges we have examined. To differentiate this mode from the quasi-regular Monami A mode, we have named it the quasi-regular Monami B mode. The variation of instability excitation position with time for the case $\gamma = 0.06$, $d = 1.2$ is shown

by the solid red line in Fig. 6(a). It is evident that the variation of instability excitation position is less regular in comparison with the quasi-regular Monami A mode. The fast Fourier transform of the inclination angle and its upper envelope yields the spectra shown in the middle and right columns of Fig. 6(b). Near the position of the instability excitation (at around $n = 20–40$), many frequencies in the low-frequency region are present, but they are multiply related to each other. This is also indicated by Fig. 6(c), where the spectrum of the instability onset position shows a dominant frequency $f_{onset} = 0.0040$ and its
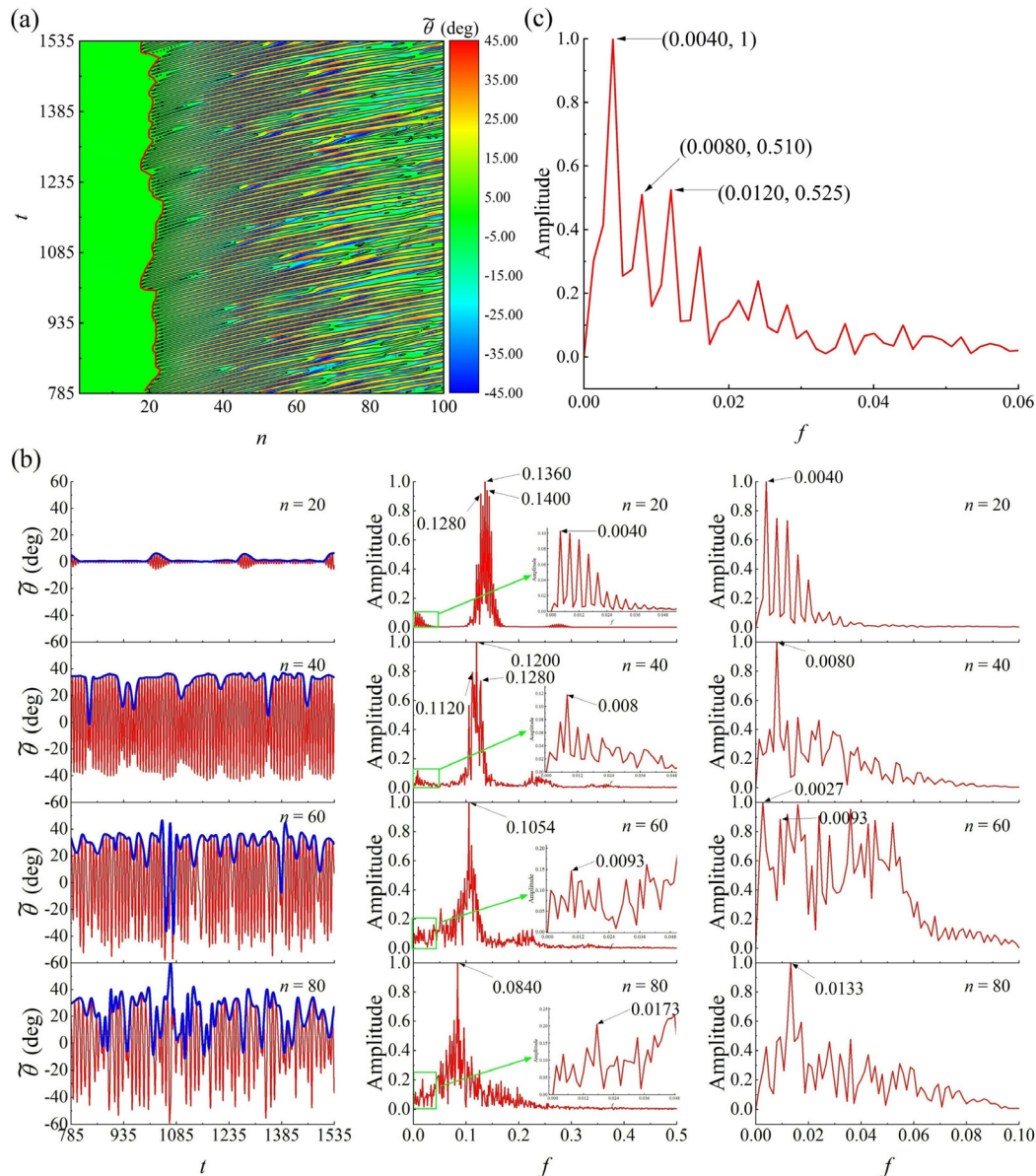

FIG. 6. (a) The spatial and temporal variations in tilt angle fluctuations across the array. (b) From left to right, the columns are time histories (solid red line) and upper envelope (solid blue line) of tilt angle fluctuations of representative vegetations, spectra of tilt angle fluctuations, and spectra of upper envelope of tilt angle fluctuations, respectively. (c) The spectrum of KH instability onset position ($\gamma = 0.06$, $d = 1.2$).

non-negligible harmonics. Clearly, in this case, the vegetation oscillation is modulated by not only the f_{onset} but also its harmonics. Furthermore, it is worth noting that the frequency of the upper envelope and the low frequency of vegetation oscillation are no longer equal from $n = 60$ onward, as shown in Fig. 6(b). This is due to the fact that in the selected case, the KH vortices can no longer be sustained and break at this position, which will be discussed in Sec. III D. In summary, the imperfect periodicity of fluctuations of the KH instability onset position leads to significant higher harmonics of f_{onset}. The

difference between mode B and A is whether the harmonics of f_{onset} are dominant or not.

For the irregular Monami mode, the case with $\gamma = 0.12$ and $d = 1.0$ is taken as an example. It can be seen from Fig. 7(a) that in the irregular Monami mode, the KH instability onset position varies irregularly with time. In the middle column of Fig. 7(b), there are multiple incommensurate frequencies with comparable intensities. The spectra of the upper envelope of the tilt angle in the right column of Fig. 7(b) and the spectrum of the fluctuation of instability onset position in
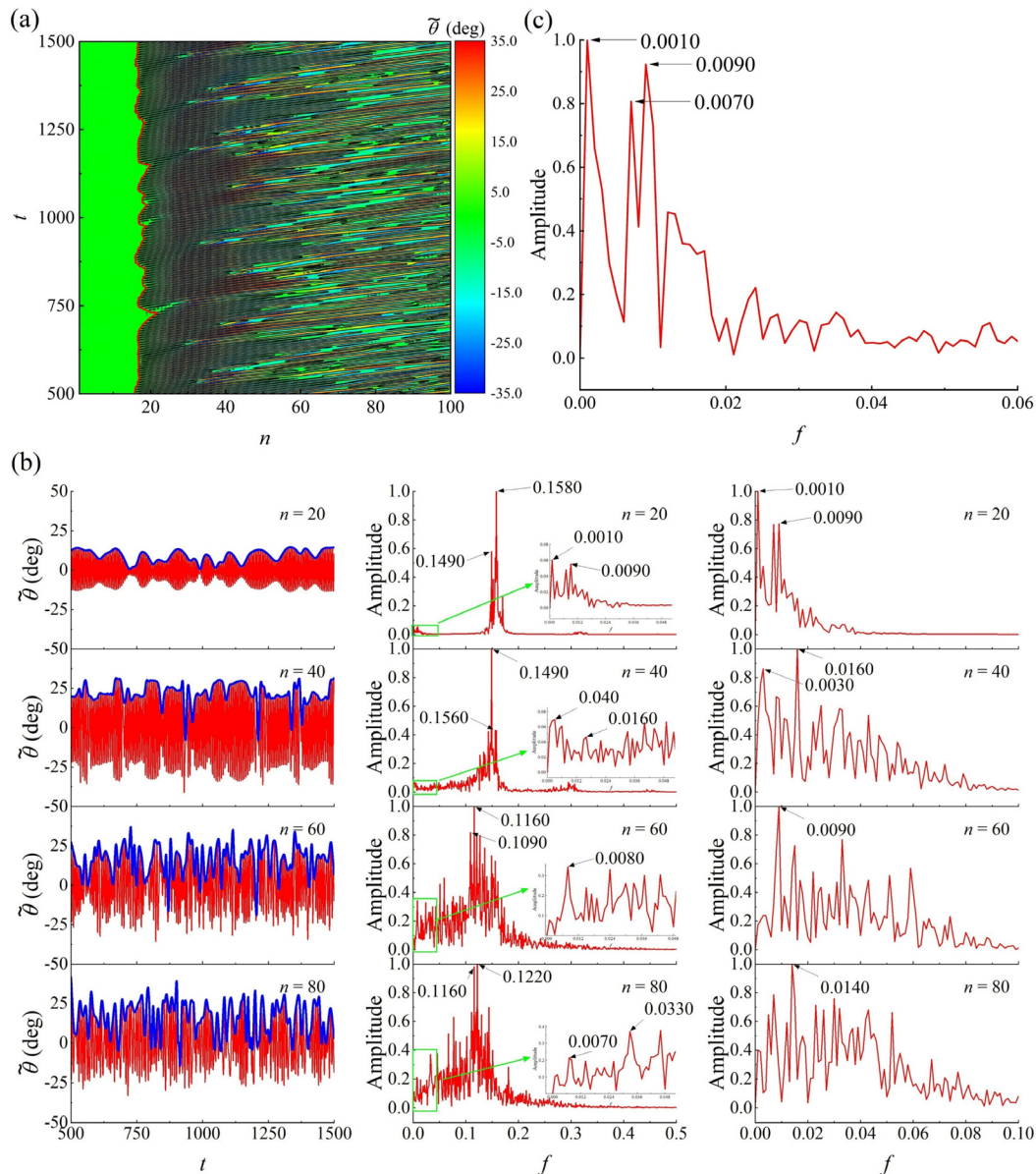

FIG. 7. (a) The spatial and temporal variations in tilt angle fluctuations across the array. (b) From left to right, the columns are time histories (solid red line) and upper envelope (solid blue line) of tilt angle fluctuations of representative vegetations, spectra of tilt angle fluctuations, and spectra of upper envelope of tilt angle fluctuations, respectively. (c) The spectrum of KH instability onset position ($\gamma = 0.12$, $d = 1.0$).

TABLE II. A summary and comparison of different Monami modes.

	Regular Monami	Quasi-regular Monami A	Quasi-regular Monami B	Irregular Monami
KH instability onset position	Fixed	Varying	Varying	Varying
The fluctuation frequency of KH instability onset position f_{onset}	None	Single frequency with negligible harmonics	Single frequency with significant harmonics	Multiple incommensurate frequencies
The oscillation of vegetation is modulated by	f_{vib}	f_{vib} and f_{onset}	f_{vib} and f_{onset}	f_{vib} and f_{onset}

Fig. 7(c) both indicate the presence of these incommensurate low-frequency components. For vegetation $n = 20$, the oscillation is modulated by the $f_{onset1} = 0.0090$, while for vegetation $n = 40$, the oscillation is modulated by the $f_{onset2} = 0.0070$. The oscillations downstream of $n = 40$ are further complicated by the complex variation of KH vortices. In other words, under irregular Monami mode, although the vegetation oscillation is still modulated by its own oscillation frequency, the fluctuation frequency of the instability onset position is no longer unique. Compared to the quasi-regular Monami modes, the oscillation of vegetation in the irregular mode is more complex. Finally, the main characteristics of different Monami modes are summarized and compared in Table II.

C. Influences of bending rigidity and gap distance on the Monami instability

As stated in the preceding section, previous studies have demonstrated that the Reynolds number, buoyancy parameter, and canopy density affect the intensity and onset position of the mixing layer. In this section, the influences of bending rigidity and gap distance on Monami instability are explored, including the effects on the Monami mode, the KH instability onset position, and the Monami characteristic scales.

The distribution of the different Monami modes in the (γ, d) parameter space is shown in Fig. 8. The figure reveals that the distribution of the Monami modes changes significantly for different bending rigidity γ and gap distance d. In the region where both γ and d are small ($0.04 \leq \gamma \leq 0.10$, $0.4 \leq d \leq 0.7$), four Monami modes with a scattered distribution are observed as there is no clearly dominant parameter. Small changes in parameters can lead to a shift in the different modes, indicating their sensitivity to parameter changes. In the region where γ is small and d is large ($0.04 \leq \gamma \leq 0.10$, $0.8 \leq d \leq 1.6$), the gap distance d plays a dominant role, and the KH instability excitation position is prone to oscillation, with only quasi-regular Monami B mode in this region. In the region where γ is larger and d is smaller ($0.12 \leq \gamma \leq 0.22$, $0.4 \leq d \leq 0.7$), the increased γ makes the mixing layer more stable, and the KH instability excitation positions are less likely to oscillate, with mostly regular Monami modes in this region and only a few quasi-regular Monami modes scattered around the boundaries. When both γ and d are large, all modes are present except for the quasi-regular Monami A mode, and the transition between modes is closely related to γ and d. The diagonal green dashed line is taken as the dividing line where the two parameters have an equal effect. Near this line, the vegetation arrays exhibit an irregular Monami mode due to the competition of γ and d. Moving away from the line in the direction of increasing γ, the dynamic mode changes
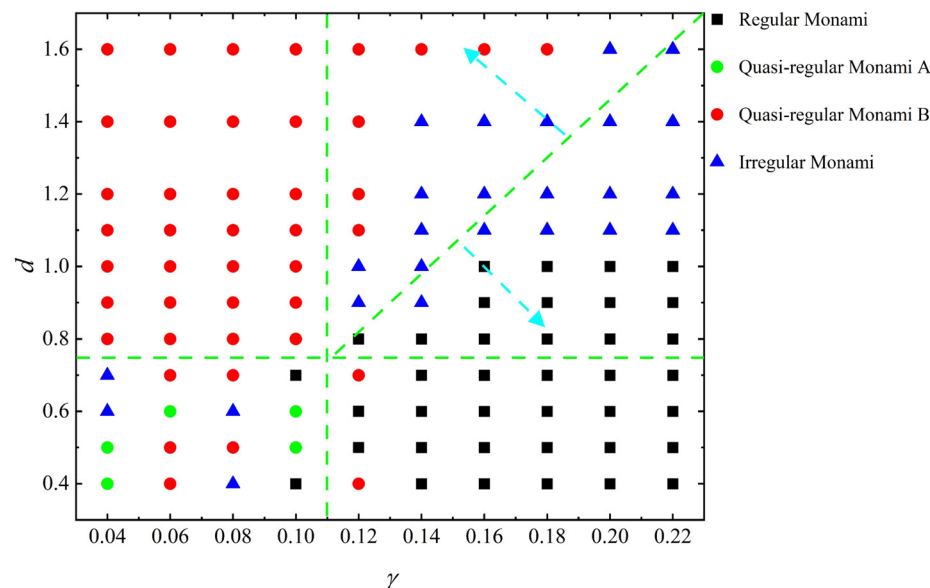
FIG. 8. A map for the classification of Monami modes in the space of (γ, d). The black squares, green circles, red circles, and blue triangles denote the regular Monami mode, quasi-regular Monami A mode, quasi-regular Monami B mode, and irregular Monami mode, respectively.

from irregular Monami to regular Monami, while moving away from the line in the direction of increasing d, the dynamic mode transitions from irregular Monami to quasi-regular Monami B mode. In general, it is found that higher rigidity and smaller gap distance lead to a fixed pattern of KH instability onset and thus, regular Monami waves are observed for such vegetation patterns. Lower rigidity and larger gap distance lead to a quasi-regular B pattern of KH instability onset; thus, quasi-regular Monami B modes are presented. On the other hand, both higher rigidity and larger gap distance and lower rigidity and smaller gap distance can lead to different KH instability onset patterns and thus cause different Monami modes, and especially, KH instability onset patterns and the corresponding Monami modes are extremely sensitive to lower rigidity and smaller gap distance.

The characteristics of the KH instability onset position, such as the mean value and its standard deviation, are clearly influenced by the bending rigidity γ and gap distance d. As shown in Fig. 9(a), it can be seen that the mean value of the instability onset position decreases as the gap distance increases, i.e., the instability onset position moves upstream, which is consistent with the findings of Fang et al.[23] As the bending rigidity increases, the onset position also shifts upstream. This means that γ and d play the same role in shifting the mean onset position. When both bending rigidity and gap distance are small ($0.04 \leq \gamma \leq 0.10$, $0.4 \leq d \leq 0.6$), the instability onset position moves sharply upstream with increasing γ and d, up to a maximum of $\Delta n = 30$. Further increasing γ or d results in a smaller upstream shift of the onset position, about $\Delta n = 10$. When both bending rigidity and gap distance are large ($0.16 \leq \gamma \leq 0.22$, $1.0 \leq d \leq 1.6$), the onset position is more stable, and changing γ and d has an insignificant shift, $\Delta n < 5$, in the onset position.

The variation of the standard deviation of the onset position is given in Fig. 9(b). It can be seen that the variation of the standard deviation is closely related to the Monami mode. In the range of $0.04 \leq \gamma \leq 0.10$ and $0.8 \leq d \leq 1.6$, dominated by the quasi-regular Monami B mode, the standard deviation decreases with increasing bending rigidity. However, the variation with the gap distance is complicated. In the range of $0.14 \leq \gamma \leq 0.22$ and $0.4 \leq d \leq 0.7$, the standard deviation is zero because of the prevailed regular Monami mode in which the onset position is constant. In the other regions, due to the mode transition, the standard deviation varies intricately with γ and d and is not further discussed here.

In addition to the mean and standard deviation of the KH instability onset position, it is also important to consider the upstream and downstream boundaries, i.e., the most upstream and downstream positions that can be reached, when describing how the onset position fluctuates. Figures 10(a) and 10(b) show the variation of the upstream and downstream boundaries of the onset position in the (γ, d) parameter space, respectively. It can be seen that the variation of the upstream boundary of the onset position follows the same trend as the mean onset position. However, for the downstream boundary, the variation with respect to γ and d is more complex, indicating that the downstream boundary is more sensitive to these parameters and the Monami modes.

At the end of this section, the distributions of Monami mean wavelength and mean wave height in the parameter space are given according to the definitions in Sec. III A, and their variations with the parameters are explored and compared with the results in the literature. As shown in Fig. 11(a), the Monami mean wave height $\overline{H}_m$ is significantly affected by bending rigidity γ, while it is less affected by the gap distance d. Note that the axes in this figure are switched in comparison with Figs. 9 and 10 to present the variations of the mean wave height and mean wavelength more clearly. In general, $\overline{H}_m$ decreases gradually with increasing γ, and the larger the gap distance, the larger the decrease. In the range of $0.18 \leq \gamma \leq 0.22$, $\overline{H}_m$ is very small, and changing the bending rigidity has almost no effect on it. As seen from Fig. 11(a), $\overline{H}_m$ increases with increasing d at small values of γ. However, it is marginally affected by the gap distance when the bending rigidity is high. The Monami mean wavelength $\overline{L}_m$ is also significantly affected by both γ and d. As shown in Fig. 11(b), $\overline{L}_m$ mildly decreases with increasing γ, while it sharply increases with increasing d, and this increase is particularly pronounced in the range of $1.2 \leq d \leq 1.6$. In summary, Monami wave height and wavelength decrease with increasing bending rigidity and increase with increasing gap distance, consistent with the findings of Wang et al.[20] However, the mean wave height relies more on the bending rigidity, while the mean wavelength depends more on the gap distance.
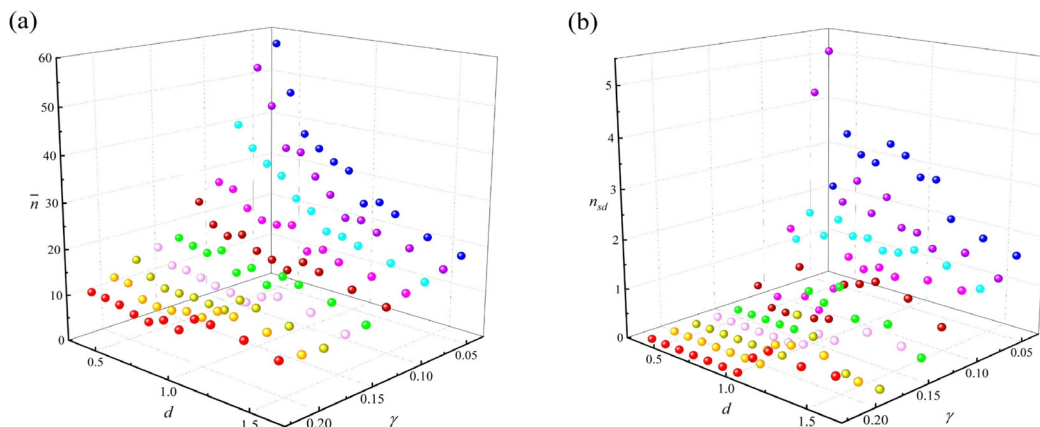

FIG. 9. Variations of the (a) mean and (b) standard deviation of the KH instability onset position with bending rigidity γ and gap distance d. The same color indicates the same bending rigidity γ.

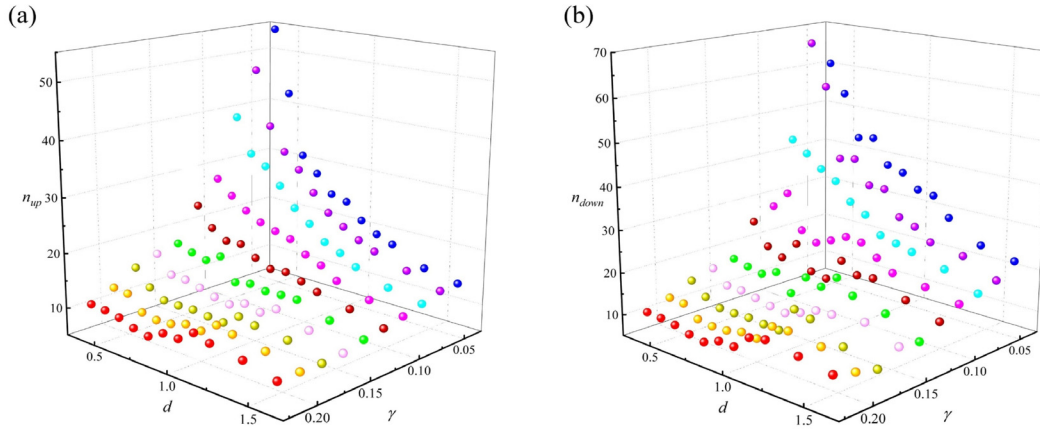**FIG. 10.** Variations of the (a) upstream boundary and (b) downstream boundary of the KH instability onset position with bending rigidity γ and gap distance d. The same color indicates the same bending rigidity γ.

D. The spatial and temporal variations of the Monami characteristic scales in different Monami modes

Section III C discusses the distributions of the space and time-averaged features of the KH instability onset position and Monami characteristic scales in the parameter space. However, the Monami characteristic scales also experience spatial and temporal variations. This section investigates the spatial and temporal variations of the Monami characteristic scales for four different Monami modes and explains the underlying physics.

For the regular Monami mode, the spatiotemporal variations of wave height and wavelength are shown in Figs. 12(a) and 12(b), respectively, for the case $\gamma = 0.2$ and $d = 0.4$, with the red solid line indicating the location of the instability excitation. The wave height shows a first-increase-then-decrease variation with spatial position. Near the instability onset position, the KH vortex is initially excited with a small size and low intensity, resulting in a small wave height as shown in Fig. 3(a). As the KH vortices develop and increase in size and intensity, the Monami wave height gradually increases and

reaches a maximum at around $n = 30$–40. After this, the KH vortex gradually moves upward away from the vegetation and reaches a matured size. As it continues to move downstream, the KH vortex gradually dissipates and loses strength due to fluid viscous effects. Because of the uplifted and weakened KH vortex, the oscillation of the vegetation decreases, resulting in a decrease in the Monami wave height.

As for wavelength, the Monami wavelength after $n = 40$ is significantly larger than that before $n = 40$, and the wavelength varies less in the region with $n > 40$. This can be explained by the fact that the scales of KH vortices after $n = 40$ are almost fixed and larger than those before $n = 40$, which is also reflected by the tilt angle fluctuation results shown in Fig. 4(a). Since the angle between the stripes and the ordinate axis is related to the wave velocity c, it can be seen from Fig. 4(a) that the wave velocity downstream of the array is slightly greater than that upstream, due to the higher velocity flow away from the vegetation, which convects the KH vortices faster when they are uplifted in the downstream. However, the vegetation oscillation
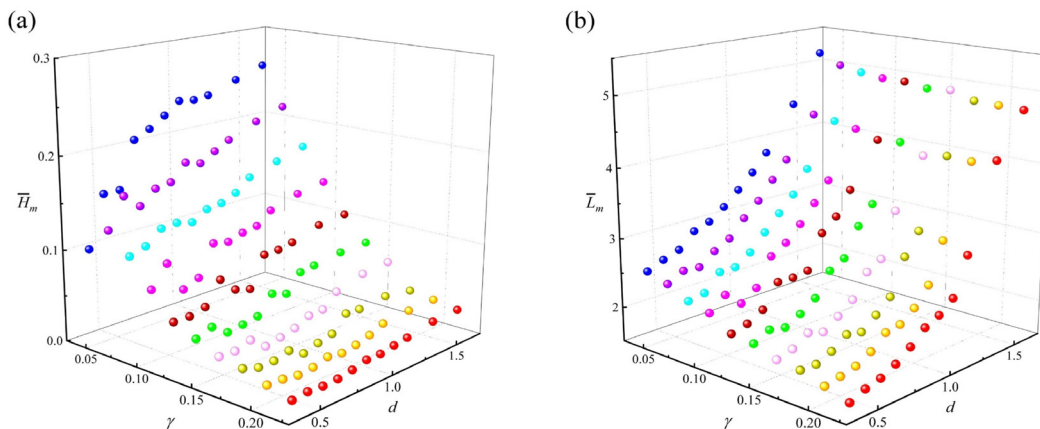

FIG. 11. Variations of the (a) mean wave height and (b) mean wavelength of Monami with bending rigidity γ and gap distance d. The same color indicates the same bending rigidity γ.
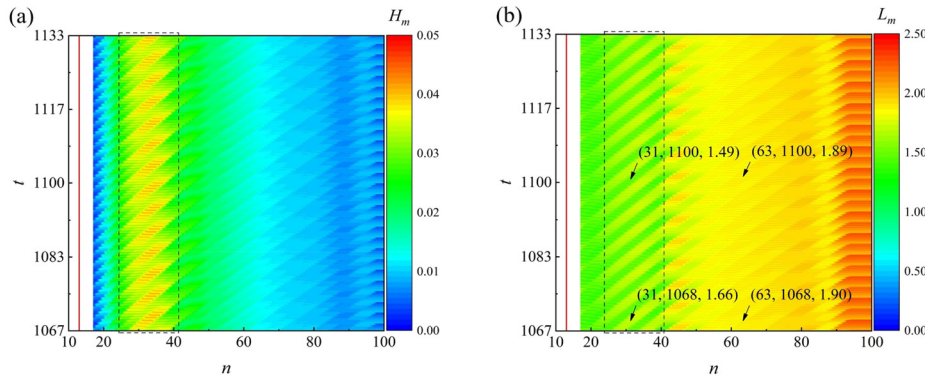
FIG. 12. The spatial and temporal variations in Monami (a) wave height and (b) wavelength across the array in the regular Monami mode ($\gamma = 0.2$, $d = 0.4$). The solid red line and the dashed black box indicate the KH instability onset position and the region where the stripes exist, respectively.

period, i.e., the Monami waving period T in the regular mode, is equal in the upstream and downstream. According to $L = cT$, it can be obtained that the Monami wavelength downstream of the array is larger than that upstream.

It is also worth noting that the spatiotemporal variations of wave height and wavelength show a streaky pattern in the range of about $n = 25$–40, as shown by the black dashed boxes in Figs. 12(a) and 12(b). This implies that the wave height and wavelength are constantly changing in this region. Take the vegetation $n = 31$ as an example, where the KH vortex is not yet completely detached from the vegetation array. When the vegetation is located between two adjacent KH vortices, as shown in Fig. 13(a), the wavelength is $L_{m1} = 1.66$. However, when the vegetation is subjected to the direct action of the KH vortex, as shown in Fig. 13(b), the wavelength is $L'_{m1} = 1.49$. As the vegetation periodically experiences both "gap" and "direct action," the Monami wave alternates between large and small wavelengths at different times, resulting in stripes in the spatial and temporal diagram of wavelengths. When the KH vortex is completely detached from the vegetation array, at $n = 63$, for example, the wavelengths at which the vegetation is located are approximately equal, i.e., $L_{m2} \approx L'_{m2} = 1.90$, regardless of whether the vegetation is located directly below the KH vortex or between two adjacent KH vortices. The same is true for the

variation in the wave height. That is to say, in the regular Monami mode, the spatial and temporal variations of the Monami characteristic scales are the results of KH vortex evolution along the array.

For the quasi-regular Monami A mode, the spatiotemporal variations of wave height and wavelength at $\gamma = 0.06$ and $d = 0.6$ are given in Figs. 14(a) and 14(b), respectively. The red solid line indicating the KH instability onset position fluctuates roughly between $n = 32$–40. It can be seen from the figure that the spatiotemporal variation of Monami wave height and wavelength shows an obvious periodicity, which is closely related to the fluctuation of the instability onset position. In the following, the variation of Monami wave height in Fig. 14(a) is taken as an example to elaborate on the mechanisms behind this phenomenon, and the same applies to the variation of wavelength.

When the instability onset position is near $n = 32$, the KH vortex is excited at a position where the boundary layer thickness is relatively thin. As a result, the excited KH vortex has a larger horizontal velocity u and a higher height of vortex core when it passes by a given vegetation, compared with the vortices excited at other times (i.e., at other positions), as shown in Fig. 15(a) for vortex 1. The higher position of the vortex core causes vortex 1 to penetrate less deeply and interact less with the vegetation, forming a small wave height everywhere it passes [see the blue spikes in Fig. 14(a)], which continues until around
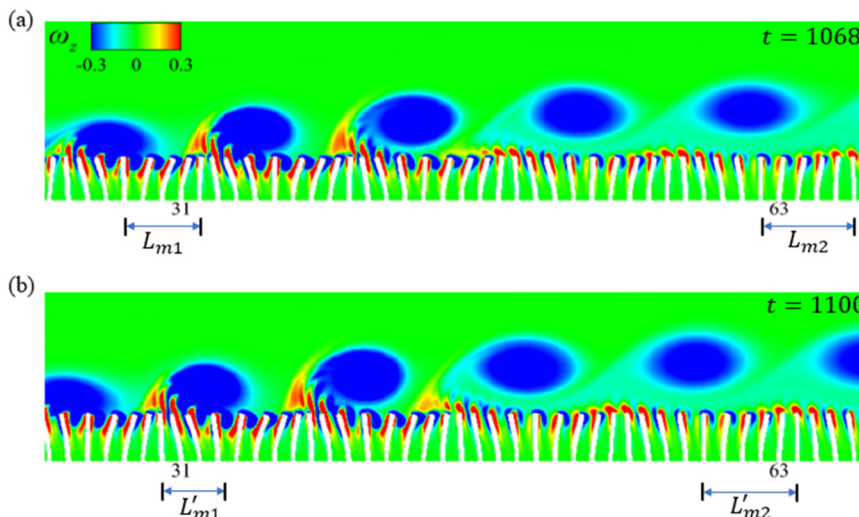

FIG. 13. Contours of z-vorticity at (a) $t = 1068$ and (b) $t = 1100$. L_{m1} and L'_{m1} represent wavelengths for $n = 31$ at $t = 1068$ and 1100, respectively. L_{m2} and L'_{m2} represent wavelengths for $n = 63$ at $t = 1068$ and 1100, respectively.
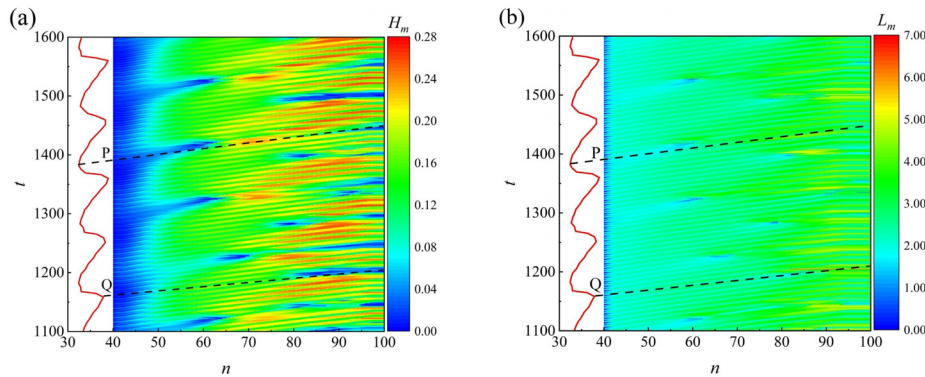
FIG. 14. The spatial and temporal variations in Monami (a) wave height and (b) wavelength across the array in the quasi-regular Monami A mode ($\gamma = 0.06$, $d = 0.6$). The solid red line and the dashed black lines indicate the KH instability onset position and the process of the KH vortex propagating downstream, respectively.

$n = 60$. The larger u makes vortex 1 move faster than the vortices generated at other times, thus catching up with the previous vortex, i.e., vortex 2, near the 65th vegetation, as shown in Fig. 15(b). This merging results in an instantaneous increase in the wave height around $n = 70$, as shown in Fig. 14(a). As vortex 1 and vortex 2 slow down during the merging, the two are caught up and merge again with vortex 3, forming vortex 4 and vortex 5. Actually, vortex 5 consists of a vortex pair with opposite rotational directions and an upward gap flow in between, due to which vortex 5 breaks away from the array near $n = 85$, as shown in Figs. 15(e) and 15(f). As a result, the sweep effect on the vegetation is significantly weaker, and a small wave height appears in the last part of the array. The above-mentioned process is shown by the dashed black line P in Fig. 14.

When the onset position is near $n = 40$, the KH vortex excited here moves at a lower speed due to the thicker boundary layer, as shown by vortex 1 in Fig. 16(a). In this case, vortex 1 is caught up and merges with vortex 2 near $n = 85$, as shown in Figs. 16(b) and 16(c). However, the merged vortex 4 moves very slowly and is soon caught up again by vortex 3 behind it. A shear layer, which is unstable and is briefly maintained before rapidly rolling up, is thus formed locally, creating a small wave height at the end of the vegetation array, as shown

in Fig. 16(d). The above process is shown by the dashed black line Q in Fig. 14.

The above-mentioned analysis suggests that changes in the position of the KH instability onset lead to KH vortices generating at different thicknesses of the boundary layer. This results in variations in the convection velocities of the KH vortices and the positions and patterns of their merging as they move downstream. Therefore, the spatial and temporal variations in the Monami characteristic scales in the quasi-regular Monami A mode are closely related to the fluctuations in the KH instability onset position. The regular variation in the onset position leads to periodic patterns of vortex merging, resulting in the regular variation of Monami wave height and wavelength.

Figure 17(a) shows the spatiotemporal variation of the wave height in the case where $\gamma = 0.06$ and $d = 1.2$ for the quasi-regular Monami B mode. It is evident that the variation of wave height with the KH instability onset position is more complex because the fluctuation of the onset position is no longer regular. However, there is still some periodicity in this complex variation, particularly in the range of $n = 24$–40, as indicated by the black dashed circles in this figure. It is not difficult to determine that this periodicity occurs at a frequency of approximately $f = 0.0080$, which matches well with the fluctuation
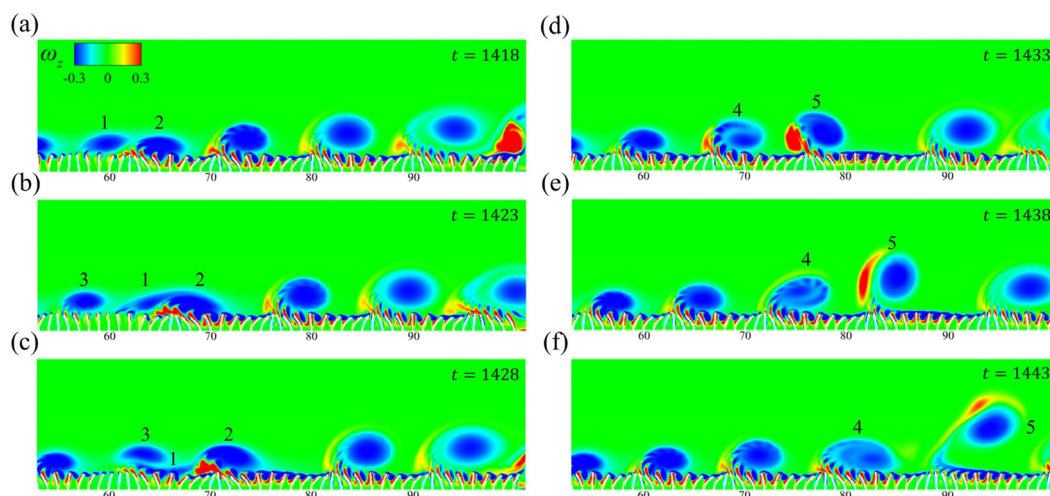

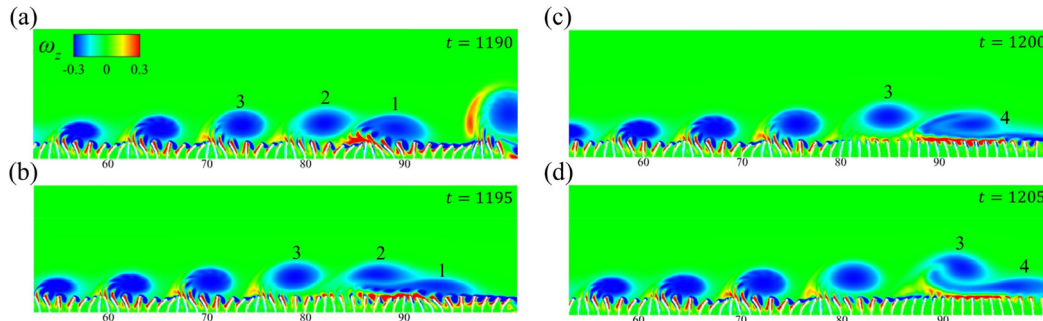**FIG. 15.** Contours of z-vorticity representing process P in Fig. 14 from $t = 1418$ to 1443.

FIG. 16. Contours of z-vorticity representing process Q in Fig. 14 from $t = 1190$ to 1205.
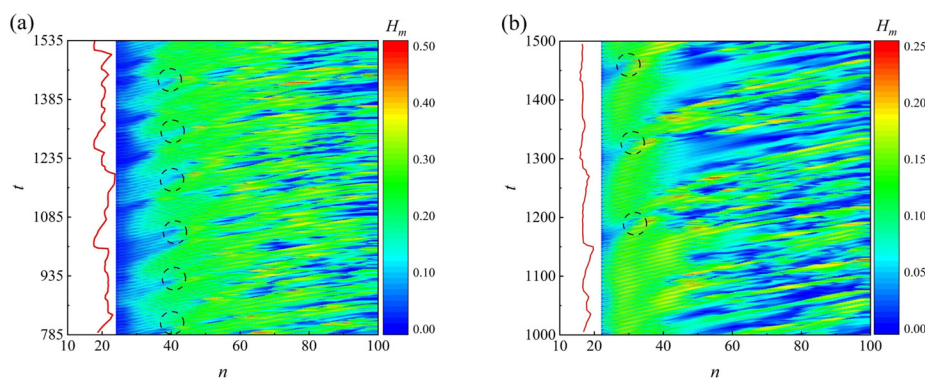

FIG. 17. The spatial and temporal variations in the Monami wave height across the array in (a) the quasi-regular Monami B mode ($\gamma = 0.06$, $d = 1.2$) and (b) the irregular Monami mode ($\gamma = 0.12$, $d = 1.0$). The solid red line and dashed black circles indicate the KH instability onset position and some periodic variations in wave height, respectively.

frequency of the KH instability onset position in this case. This means that the variation of the Monami wave height in this range is still governed by the onset position. However, in the range of $n = 50$–100, the wave height variation is very complex and exhibits no trace of periodicity. This is primarily due to the fact that, at this downstream position, the KH vortex continues to dissipate during its convection and cannot continue to hold and breaks up near $n = 60$, thus making the vortex field downstream of this position chaotic and disordered, as shown in Fig. 18(a). The complex variation in the Monami wave height is mainly caused by the chaotic flow field. A similar situation arises in the irregular Monami mode. Figure 17(b) presents a plot of the spatiotemporal variation of the wave height for the case where $\gamma = 0.12$ and $d = 1.0$. In the range of $n = 22$–40, the "periodic" variation marked by

the black dashed circles occurs at a frequency of 0.0071, which is one of several KH instability onset frequencies (0.0010, 0.0070, and 0.0090). However, the so-called periodicity does not persist for an extended period, and it disappears during $t = 1000$–1150. That is to say, the variation of the Monami wave height is only partially controlled by the KH instability onset position in this range. Downstream of this range, the wave height variation and the vortex evolution exhibit no periodicity at all, similar to the quasi-regular Monami B mode, as shown in Figs. 17(b) and 18(b). In summary, the spatiotemporal variations of the Monami characteristic scales in these two Monami modes are modulated by the fluctuation of the KH instability onset position and complex interactions between vortices at different temporal and spatial scales.
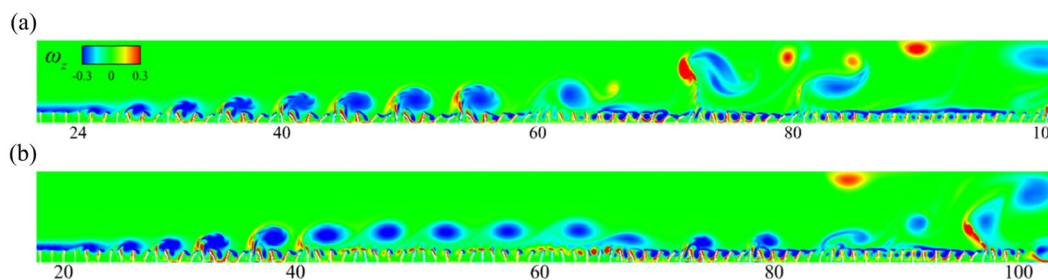

FIG. 18. Contours of instantaneous z-vorticity in (a) the quasi-regular Monami B mode ($\gamma = 0.06$, $d = 1.2$) and (b) the irregular Monami mode ($\gamma = 0.12$, $d = 1.0$).

IV. CONCLUSION

Direct numerical simulations were conducted to investigate the behavior of a large array of flexible vegetations submerged in a 2 D laminar boundary-layer flow. The simulations used the immersed boundary method with a parameter combination of Re = 400, $\beta = 1.0$, $\gamma = 0.04$–0.22, and $d = 0.4$–1.6. The time histories and spectra of inclination angle fluctuations and their upper envelope, as well as the spectra of fluctuation of KH instability onset position, were analyzed to identify four Monami modes: regular Monami, quasi-regular Monami A, quasi-regular Monami B, and irregular Monami. The influences of the bending rigidity and gap distance on the Monami modes, KH instability onset position, and Monami characteristic scales were discussed in detail. The causes of spatial and temporal variations of the Monami characteristic scales in different Monami modes were also elucidated.

The fluctuation frequency of the KH instability onset position modulates the Monami modes, resulting in different dynamic features. In regular Monami, the vegetations oscillate at a single frequency because the KH instability onset position remains fixed. For quasi-regular Monami A, the modulation of onset position fluctuation frequency induces different oscillation frequencies of vegetations. Quasi-regular Monami B is modulated by both the fluctuation frequency of onset position and its higher harmonics, while irregular Monami is modulated by multiple incommensurate frequencies of onset position fluctuation.

The Monami modes, onset position, and Monami scales are influenced by the bending rigidity and gap distance. The mean value of KH instability onset position moves upstream with increasing bending rigidity and gap distance due to the joint upstream shift of both the upstream and downstream boundaries. The standard deviation of the onset position mostly relies on its corresponding Monami mode. Moreover, the mean Monami wave height and wavelength decrease with the increasing bending rigidity, while they increase with the increasing gap distance.

The causes of spatial and temporal variations of the Monami characteristic scales differ across the four modes. In the regular Monami mode, spatial and temporal variations are a result of KH vortex evolution along the array. In the quasi-regular Monami A mode, the regular variation of onset position causes different vortex merging patterns occurring at different positions over a fixed period, leading to regular spatiotemporal variations of Monami scales. In quasi-regular Monami B and irregular Monami modes, some periodicity appears in the spatiotemporal variations of Monami scales near the onset position due to the onset position fluctuation, while the complex interactions between vortices play an important role far from the onset position.

Overall, this study reveals a new underlying mechanism that the fluctuation of KH instability onset position has an influence on the Monami phenomenon, which has never been discussed quantitatively in previous studies. The frequency of KH instability onset position fluctuation is manifested as a low frequency in Monami, based on which four Monami modes are classified. In general, the mean onset position moves upstream with increasing bending rigidity and gap distance. The temporal variations of this onset position can lead to spatial and temporal variations of the Monami characteristic scales. The fluctuation of KH instability onset position should be paid more attention in future studies of similar flows since KH instability and its vortices affect the vertical transport of momentum, vertical scalar fluxes, mean velocity profile, as well as turbulent diffusivity. Our analysis is therefore expected to have a wider impact in other related scenarios.

AUTHOR DECLARATIONS
Conflict of Interest

The authors have no conflicts to disclose.

Author Contributions

Jinyuan Ni: Conceptualization (equal); Data curation (lead); Formal analysis (equal); Validation (lead); Visualization (lead). **Chunning Ji:** Conceptualization (equal); Formal analysis (equal); Methodology (lead); Resources (equal); Supervision (equal); Writing – review & editing (equal). **Dong Xu:** Resources (equal); Supervision (equal); Writing – review & editing (equal). **Xing Zhang:** Writing – review & editing (equal). **Dongfang Liang:** Writing – review & editing (equal).

DATA AVAILABILITY

The data that support the findings of this study are available from the corresponding author upon reasonable request.

APPENDIX: NUMERICAL METHODOLOGY VALIDATION AND ARRAY LENGTH AND MESH GRID INDEPENDENCE TESTS

To verify the accuracy of the present numerical methodology, numerical simulations were performed at Re = 400, $\gamma = 0.2$, $d = 0.5$, and $V = 90$, and the results were compared with those of Zhang
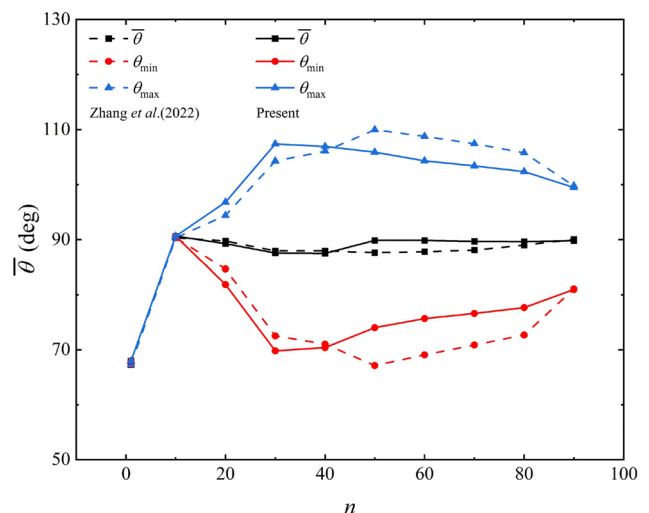

FIG. 19. Comparison of the mean, minimum, and maximum values of the inclination angle for selected representative vegetations with $\gamma = 0.2$, $d = 0.5$, $\beta = 1.0$, Re = 400, and $V = 90$.
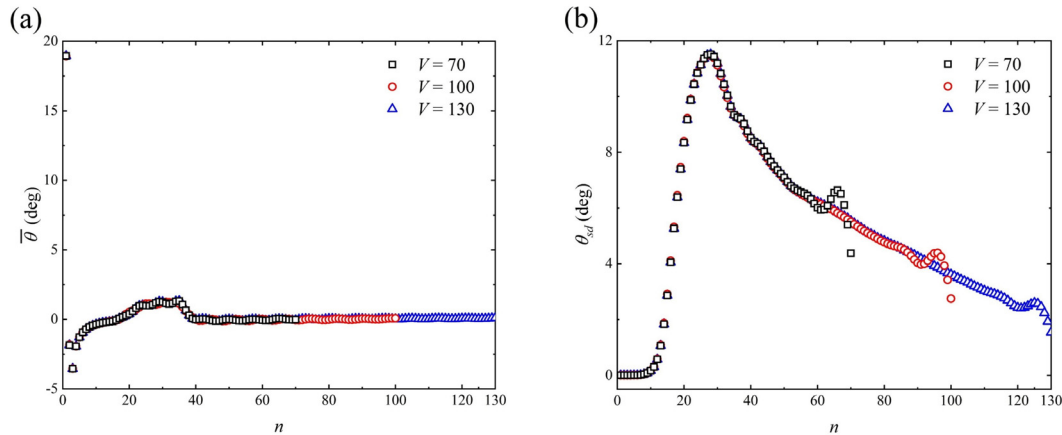
08 August 2023 02:15:50

FIG. 20. Results of the array length independence test. (a) The mean and (b) standard deviation of the inclination angle along the array by using a different number of vegetations in the array. The black square, red circle, and blue triangle represent the results for the vegetations number of 70, 100, and 130, respectively.
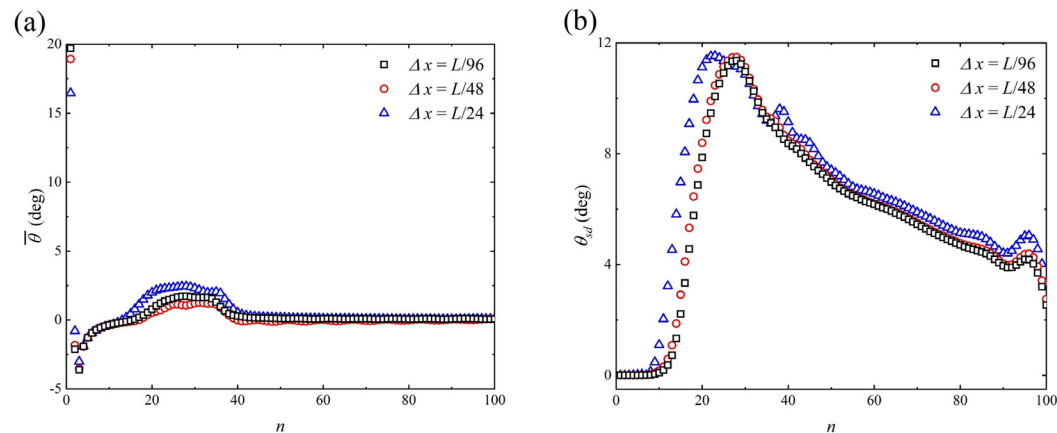

FIG. 21. Results of the mesh size independence test. (a) The mean and (b) standard deviation of the inclination angle along the array by using different meshes. The black square, red circle, and blue triangle represent the results for the mesh size of $L/96$, $L/48$, and $L/24$, respectively.

et al.[19] using the same setups. Figure 19 displays the comparison of the mean ($\bar{\theta}$), minimum (θ_{min}), and maximum (θ_{max}) values of inclination angle for selected representative vegetations. The results indicate that the differences between the present results and those of Zhang et al.[19] fall within a reasonable range, thus confirming the accuracy of the present numerical methodology.

To ensure that the FSI simulation results in the present study are independent of the number of vegetations in the array and the mesh resolution, tests were conducted on a representative case with $\gamma = 0.2$, $d = 0.5$, $\beta = 1.0$, and Re $= 400$.

Figures 20(a) and 20(b) show the mean value and standard deviation of the inclination angle for each vegetation along the array under three cases of $V = 70$, $V = 100$, and $V = 130$. From the figures, it can be seen that adding more vegetations to the array has almost no effect on $\bar{\theta}$, and it only affects θ_{sd} near the end of the array. Figure 20(b) also shows that no matter how much the number of vegetations V is increased, from 70 to 100 or to 130, the slope of θ_{sd} downstream of the array remains almost constant. To study a longer array of vegetations with as little computational effort as possible, the number of vegetations $V = 100$ is selected in the simulations.

Similarly, a mesh grid independence test was conducted on the same case with an array length of $V = 100$. Figure 21 shows that both $\bar{\theta}$ and θ_{sd} have significantly smaller discrepancies between $\Delta x = L/96$ and $\Delta x = L/48$ than between $\Delta x = L/48$ and $\Delta x = L/24$. In view of the convergence, the grid width $\Delta x = L/48$ is used in the present study.

REFERENCES

[1]S. R. Carpenter and D. M. Lodge, "Effects of submersed macrophytes on ecosystem processes," Aquat. Bot. **26**, 341–370 (1986).
[2]V. S. Neary, S. G. Constantinescu, S. J. Bennett, and P. Diplas, "Effects of vegetation on turbulence, sediment transport, and stream morphology," J. Hydraul. Eng. **138**(9), 765–776 (2012).
[3]K. A. Moore, "Influence of seagrasses on water quality in shallow regions of the lower Chesapeake Bay," J. Coastal Res. **2009**(10045), 162–178 (2004).

[4]L. N. Augustin, J. L. Irish, and P. Lynett, "Laboratory and numerical studies of wave damping by emergent and near-emergent wetland vegetation," Coastal Eng. **56**(3), 332–340 (2009).

[5]K. B. Gedan, M. L. Kirwan, E. Wolanski, E. B. Barbier, and B. R. Silliman, "The present and future role of coastal wetland vegetation in protecting shorelines: Answering recent challenges to the paradigm," Clim. Change **106**(1), 7–29 (2011).

[6]L. Xie and Y. Zhu, "Scour protection of underwater pipelines," J. Civ. Eng. Constr. **7**(4), 171 (2018).

[7]J. D. Ackerman and A. Okubo, "Reduced mixing in a marine macrophyte canopy," Funct. Ecol. **7**(3), 305–309 (1993).

[8]E. D. Langre, "Effects of wind on plants," Annu. Rev. Fluid Mech. **40**(1), 141–168 (2008).

[9]M. Ghisalberti and H. M. Nepf, "Mixing layers and coherent structures in vegetated aquatic flows," J. Geophys. Res.: Oceans **107**(C2), 3-1–3-11, https://doi.org/10.1029/2001JC000871 (2002).

[10]S. Patil, V. P. Singh, and A. K. Rastogi, "Linear instability theory for frequency assessment of coherent vortices in submerged and aside rigid canopies," J. Hydrol. Eng. **15**(12), 1023–1029 (2010).

[11]C. Y. H. Wong, P. H. Trinh, and S. J. Chapman, "Shear-induced instabilities of flows through submerged vegetation," J. Fluid Mech. **891**, A17 (2020).

[12]Y. Jin, J.-T. Kim, and L. P. Chamorro, "Instability-driven frequency decoupling between structure dynamics and wake fluctuations," Phys. Rev. Fluids **3**(4), 044701 (2018).

[13]Y. Jin, J.-T. Kim, L. Hong, and L. P. Chamorro, "Flow-induced oscillations of low-aspect-ratio flexible plates with various tip geometries," Phys. Fluids **30**(9), 097102 (2018).

[14]Y. Jin, J.-T. Kim, Z. Mao, and L. P. Chamorro, "On the couple dynamics of wall-mounted flexible plates in tandem," J. Fluid Mech. **852**, R2 (2018).

[15]Y. Jin, J.-T. Kim, S. Fu, and L. P. Chamorro, "Flow-induced motions of flexible plates: Fluttering, twisting and orbital modes," J. Fluid Mech. **864**, 273–285 (2019).

[16]J. O'Connor and A. Revell, "Dynamic interactions of multiple wall-mounted flexible flaps," J. Fluid Mech. **870**, 189–216 (2019).

[17]X. Zhang, G. He, and X. Zhang, "Fluid–structure interactions of single and dual wall-mounted 2D flexible filaments in a laminar boundary layer," J. Fluids Struct. **92**, 102787 (2020).

[18]Y. Chen, J. Ryu, Y. Liu, and H. J. Sung, "Flapping dynamics of vertically clamped three-dimensional flexible flags in a Poiseuille flow," Phys. Fluids **32**(7), 071905 (2020).

[19]X. Zhang, Y. Li, and X. Zhang, "Dynamic interactions of multiple wall-mounted flexible plates in a laminar boundary layer," Front. Phys. **10**, 881966 (2022).

[20]J. Wang, G. He, S. Dey, and H. Fang, "Fluid–structure interaction in a flexible vegetation canopy in an open channel," J. Fluid Mech. **951**, A41 (2022).

[21]H. M. Nepf, "Flow and transport in regions with aquatic vegetation," Annu. Rev. Fluid Mech. **44**(1), 123–142 (2012).

[22]S. Wang, J. Ryu, J. Yang, Y. Chen, G. He, and H. J. Sung, "Vertically clamped flexible flags in a Poiseuille flow," Phys. Fluids **32**(3), 031902 (2020).

[23]Z. Fang, C. Gong, A. Revell, and J. O'Connor, "Fluid–structure interaction of a vegetation canopy in the mixing layer," J. Fluids Struct. **109**(3), 103467 (2022).

[24]D. Xu, J. Liu, Y. Wu, and C. Ji, "Numerical investigation of the dynamics of flexible vegetations in turbulent open-channel flows," J. Hydrodyn. **34**(4), 681–699 (2022).

[25]G. S. Vieira, M. R. Allshouse, and A. Mahadevan, "Seagrass deformation affects fluid instability and tracer exchange in canopy flow," Sci. Rep. **13**(1), 3910 (2023).

[26]S. Patil and V. P. Singh, "Characteristics of Monami wave in submerged vegetated flow," J. Hydrol. Eng. **15**(3), 171–181 (2010).

[27]T. Okamoto, I. Nezu, and M. Sanjou, "Flow–vegetation interactions: Length-scale of the 'monami' phenomenon," J. Hydraul. Res. **54**(3), 251–262 (2016).

[28]S. He, H. Liu, and L. Shen, "Simulation-based study of turbulent aquatic canopy flows with flexible stems," J. Fluid Mech. **947**, A33 (2022).

[29]E. C. Ting, C. Shih, and Y.-K. Wang, "Fundamentals of a vector form intrinsic finite element: Part I. Basic procedure and a plane frame element," J. Mech. **20**(2), 113–122 (2004).

[30]E. C. Ting, C. Shih, and Y.-K. Wang, "Fundamentals of a vector form intrinsic finite element: Part II. Plane solid elements," J. Mech. **20**(2), 123–132 (2004).

[31]C. Shih, Y.-K. Wang, and E. C. Ting, "Fundamentals of a vector form intrinsic finite element: Part III. Convected material frame and examples," J. Mech. **20**(2), 133–143 (2004).

[32]C. S. Peskin, "Flow patterns around heart valves: A numerical method," J. Comput. Phys. **10**(2), 252–271 (1972).

[33]C. Ji, A. Munjiza, and J. J. R. Williams, "A novel iterative direct-forcing immersed boundary method and its finite volume applications," J. Comput. Phys. **231**(4), 1797–1821 (2012).

[34]C. Ji, Y. Cui, D. Xu, X. Yang, and N. Srinil, "Vortex-induced vibrations of dual-step cylinders with different diameter ratios in laminar flows," Phys. Fluids **31**(7), 073602 (2019).

[35]W. Chen, C. Ji, M. M. Alam, J. Williams, and D. Xu, "Numerical simulations of flow past three circular cylinders in equilateral-triangular arrangements," J. Fluid Mech. **891**, A14 (2020).

[36]Z. Zhang, C. Ji, W. Chen, Y. Hua, and N. Srinil, "Influence of boundary layer thickness and gap ratios on three-dimensional flow characteristics around a circular cylinder in proximity to a bottom plane," Ocean Eng. **226**(4), 108858 (2021).

[37]W. Chen, C. Ji, M. M. Alam, D. Xu, H. An, F. Tong, and Y. Zhao, "Flow-induced vibrations of a D-section prism at a low Reynolds number," J. Fluid Mech. **941**, A52 (2022).

[38]D. Xu, J. Liu, Y. Wu, and C. Ji, "A high-efficiency discretized immersed boundary method for moving boundaries in incompressible flows," Sci. Rep. **13**(1), 1699 (2023).

[39]Z. M. Zhang and C. N. Ji, "Spacing effect on the vortex-induced vibrations of near-wall flexible cylinders in the tandem arrangement," Phys. Fluids **34**(9), 097123 (2022).

[40]G. B. Schubauer and H. K. Skramstad, "Laminar boundary-layer oscillations and transition on a flat plate," J. Res. Natl. Bur. Stand. **38**(2) (1947).

[41]V. Kulish, M. Skote, and V. Horak, "A model of laminar-turbulent transition based on viscous stream buckling," AIP Conf. Proc. **1493**(1), 590–594 (2012).

08 August 2023 02:15:50